Infrared wire grid polarizers: metrology and modeling

Matthew C. George*, Jonathon Bergquist, Rumyana Petrova, Bin Wang, Eric Gardner

Moxtek Inc., 452 W 1260 N, Orem, UT, USA;

ABSTRACT

Broad and narrow-band wire grid polarizer (WGP) products suitable for MWIR and LWIR applications requiring high contrast were developed on antireflection (AR) coated silicon using Moxtek nanowire patterning capabilities. Accurate metrology was gathered in both transmission and reflection from the SWIR to LWIR using a combination of FTIR and dispersive spectrometers, as well as laser-based light sources. The WGP structures were analyzed using SEM, FIB, and STEM techniques and optical data was derived from IR VASE, transmission, and reflectance measurements. Modeling of device performance was achieved using rigorous coupled wave analysis. Laser damage thresholds were determined and various damage mechanisms identified.

Keywords: wire grid polarizer, nanofabrication, sub-wavelength optics, form birefringence, laser damage threshold, MWIR, LWIR, thermal IR

1. INTRODUCTION

The wire grid polarizer (WGP) remains one of the most useful optical components in the field. Widely used in applications such as displays, imaging, sensors, communications, and spectroscopy, the wire grid polarizer (WGP) consists of an array of metallic lines with sub-wavelength pitch, often supported by a transparent substrate. Wire grid structures are known to be effective as infrared polarizers with several benefits over competing designs, including a compact form factor, the ability to accept a large cone angle with minimal performance variation over broad bandwidths, and improved stability over organic polarizers in high temperature and high brightness environments.[1-2] Existing WGP products designed for mid-wavelength IR and long-wavelength thermal IR applications typically suffer from low contrast between transmission of linearly polarized light in the passing and blocking configurations, which is due to their relatively large wire grid pitch (typically ≥ 370 nm). Moxtek and others have previously demonstrated a large increase in aluminum WGP performance at visible and ultraviolet wavelengths by reducing the pitch.[3-4] It follows that a dramatic reduction in pitch from that found in typical IR WGP products should greatly improve mid- and long-wavelength IR contrast. Moxtek has therefore developed several high contrast IR polarizers on anti-reflection (AR) coated silicon suitable for mid-wavelength IR (MWIR) and long-wavelength IR (LWIR) applications using wafer-scale aluminum nanowire patterning capabilities. The MWIR polarizer typically transmits better than 95% of the passing state between 3.8 and 5.5 μm while maintaining a contrast ratio of better than 37dB from 3-8 μm, while the broadband LWIR polarizer typically transmits between 68% and 93% of the passing polarization state between 8 and 15 μm and has a contrast ratio exceeding 38.5 dB. A narrowband AR-coated WGP for 7.5 μm wavelength transmits 94% of the passing state while maintaining a contrast ratio of better than 42dB while a polarizer being developed for the 10.6 μm CO_2 laser line shows 84% transmission in the passing state and a contrast ratio of about 45 dB.

Figure 1 depicts Moxtek aluminum WGP products on AR-coated silicon. The fine pitch (144 nm) and large rib aspect ratio (> 3:1) provide for improved transmission and dramatically higher contrast than competing WGP products. Potential applications for these MWIR and LWIR polarizers include spectroscopic measurement systems, optical isolators for industrial lasers, and polarization sensitive imaging systems for standoff detection, hyperspectral imaging, and guided missile technology. With the widespread use of lasers in defense, academia, and industry, Moxtek has pursued laser damage threshold (LDT) testing in both the passing and blocking polarizer orientations. Preliminary testing and analysis revealed that defects introduced during silicon AR-coating were limiting the LDT performance in the broadband LWIR product. The MWIR polarizer used an improved AR-coating and does not show the same damage initiation mechanism.

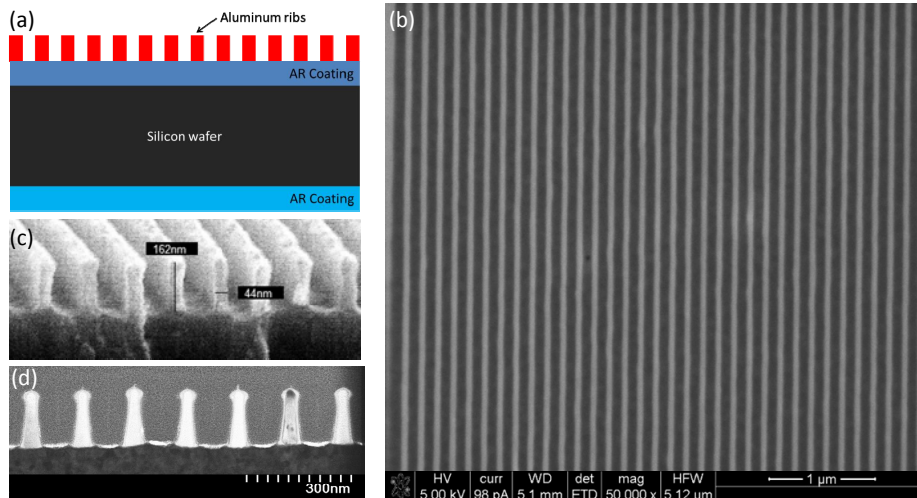*mgeorge@moxtek.com; phone 1 801 225-0930; www.moxtek.com

Figure 1. Moxtek Wire Grid Polarizers. (a) Schematic of wafer cross section (not to scale). (b)-(c) SEM images of aluminum nanowires on MWIR AR-coated silicon in (b) Plan view and (c) cross-section. (d) STEM image of rib cross-section for LWIR product after embedding in Platinum and focused ion beam milling to remove a thin section for imaging.

2. METHODOLOGY

2.1 Overview

Fourier Transform Infrared (FTIR) spectroscopic analysis of part performance in transmission was completed at Moxtek and verified at an outside reference lab. Open and blocked beam configurations and a silicon reference standard were used to validate instrument accuracy for transmission measurements. Transmission results near normal incidence were validated at a third lab by fixed wavelength measurements using a CO_2 laser. Laser Damage Threshold measurements were also completed in the passing and blocking polarizer orientations at 10.6 μm and at 3.3 μm. FTIR analysis of part performance in reflectance was completed internally and at an outside reference lab using an absolute specular reflectance accessory, but maintaining polarization purity was a challenge. Optical modeling of part performance was undertaken using the rigorous coupled wave analysis (RCWA). Sample analysis was performed using scanning electron microscopy (SEM), focused ion beam (FIB) milling, and scanning transmission electron microscopy (STEM).

2.2 FTIR transmission experiments

A Cary 670 FTIR spectrometer was used with a pre-analyzer consisting of two aligned, air-spaced Moxtek polarizers on AR-coated silicon. After nitrogen purging for 5 minutes, a background scan was taken without a sample in the compartment to establish the 100% transmittance baseline. The sample was then placed on a rotary stage and the broadband FTIR interferogram signal minimized to establish the blocking state polarizer orientation. After brief purging and measurement of the blocking state transmittance, the sample was rotated 90° and re-purged for 5 minutes before recording the passing state transmittance. This process was repeated for additional samples with intermittent measurement of the empty compartment to ensure minimal baseline drift in the single beam FTIR instrument. Blocking the beam with crossed polarizers as well as source and detector shutters could be used to establish the noise floor, though this often resulted in software errors. To ensure ordinate accuracy in the intermediate transmission ranges, a bare (uncoated) silicon reference sample was also scanned and compared to transmittance models generated from IR variable angle spectroscopic ellipsometry (IR-VASE) analysis performed by the J.A. Woollam Company. The transmission experiments were also repeated at Ball Aerospace's Optical Testing Facility using a Nexus 870 FT-IR ESP spectrometer from Thermo Nicolet and showed the same nominal behavior in the passing state and blocking states. 256 scans were averaged per spectra in the blocking polarizer configuration in order to measure a contrast ratio of 10,000 with a signal to noise ratio of approximately 5:1. High contrast for the LWIR WGP was validated at 10.6 μm using the Spica Technologies equipment described in section 2.4, while MWIR transmittance and contrast were validated between 2.7 and 3.3 μm using a CARY 5000 dual beam dispersive spectrometer. A Variable Angle Transmission Accessory from Harrick was used to measure MWIR and LWIR product transmittance at varying angle of incidence (AOI), but without a

compensating substrate to eliminate beam shifts on the detector. The sample was oriented such that the wire grid ran parallel to the vertical laboratory reference frame and the rotation axis of the sample was also parallel to the wire grid direction. As one approaches larger AOI, this configuration typically gives improved contrast in beamsplitting configurations. The blocking state polarizer transmittance (T_s) measurement was made by first fine-tuning the pre-analyzer alignment on a rotation mount to minimize the interferogram signal, and then the sample was removed for a nitrogen-purged baseline and placed back in the beam path for the T_s measurement. The pre-analyzer was then rotated 90 degrees for the nitrogen-purged, passing state transmittance (T_p) measurement and the sample was finally removed for a corrective nitrogen-purged baseline. This process was repeated for 0, 12, 20, 30, and 45° AOI Harrick stage settings.

2.3 FTIR reflection experiments

Reflectance measurements were initially performed at Ball Aerospace's Optical Testing Facility using the Thermo Nicolet FTIR spectrometer described previously, as well as a Harrick specular reflectance accessory with 12° and 45° absolute reflectance stages and a broadband WGP on Thallium Bromoiodide (KRS-5) substrate as the pre-analyzer. The specular reflectance accessory imparts a small rotation on the incoming polarization state, but for the 12° absolute reflectance stage, this polarization state is maintained between the first and second sample reflections if the sample is isotropic. For a non-isotropic medium like a WGP, the input polarization state must be rotated using a pre-analyzer to give pure *p*- or *s*-type reflections from the sample or else there will be a more complicated convolution of *p*-type, *s*-type, passing-state, and blocking-state reflectance. The 45° off-axis reflectance stage does not maintain the same polarization state between the two bounces off the sample in the "W" configuration, thus a more complicated weighting of modeling results would be necessary to make quantitative comparisons between measurements and theoretical modeling.

The rotation of the input polarization state was not properly compensated for in the initial measurement, thus the 12° AOI reflectance measurements were repeated at Moxtek using a Cary 670 FTIR spectrometer and the same Harrick reflectance accessory and stage. The same pre-analyzer described in the transmission measurements was used on a rotation mount to tune the input polarization state, which should allow for absolute measurements of R_p^2 and R_s^2. The WGP sample was placed with the part edge against the bottom reference edge of the reflectance stage such that the wires were oriented up-and-down in the laboratory reference frame. This wire orientation is orthogonal to the plane of incidence, giving *s*- and *p*-reflections for the blocked and passing polarization states respectively. The stage was placed
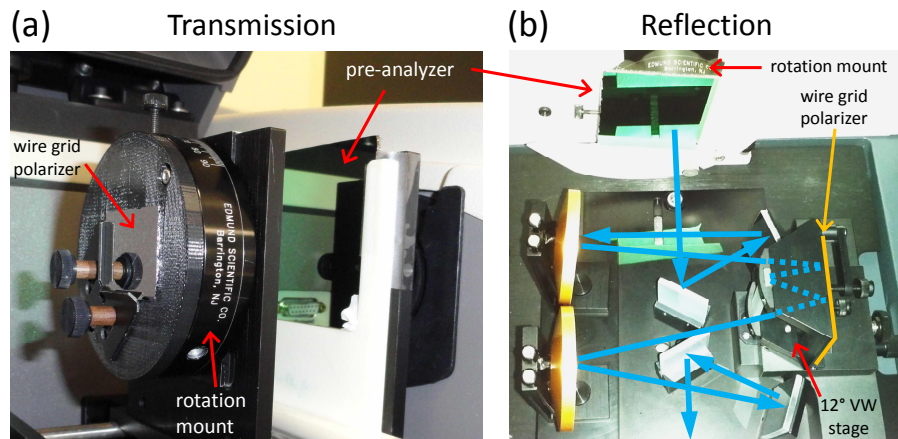

Figure 2. Measurement setups for FTIR spectroscopy in (a) normal incidence transmission and (b) reflection at 12° angle of incidence. The pre-analyzer gives broadband linearly polarized light of high purity. The rotation mount allows for fine-scale alignment of the relative orientation of the WGP and pre-analyzer.

in the "V" configuration so that beam was *transmitted* through the sample twice, then the input polarization was tuned to the blocking state by rotating the pre-analyzer to minimize the FTIR detector signal. After removing the sample, a nitrogen-purged baseline was taken in the "V" beam path configuration. The sample was then placed back on the reflectance stage and the kinematic mount flipped to generate the "W" beam path configuration (figure 2b) for measurement of the reflectance-squared in the blocking state (R_s^2). The pre-analyzer was rotated 90° for passing state reflectance measurements (R_p^2) and the sample removed for a final corrective baseline in the "V" configuration. The reflectance of an uncoated piece of double-side-polished silicon was also measured to verify instrument accuracy.

2.4 Laser damage threshold testing

For the broadband LWIR product, laser damage threshold testing was performed at a wavelength of 10.6 μm using a continuous wave Synrad Firestar CO_2 laser at Spica Technologies, Inc. The beam was focused using a convex ZnSe lens (1 m focal length) to a 360 μm $1/e^2$ spot size with a Rayleigh length of approximately 2 mm. The beam profile was measured using a calibrated aperture approach. The polarization purity of the laser beam was improved using a thin film plate polarizer designed for 10.6 μm wavelength. The beam was steered using zero-phase reflector mirrors and the laser power was attenuated using the reflective thin film plate polarizer and a partial reflector. Fine-tuning of laser output power was achieved using RF carrier wave modulation. Operating the laser at low powers led to increased carrier wave modulation of the instantaneous laser power and LDT behavior approaching that of a pulsed laser experiment. The CO_2 laser was thus operated at high power to reduce the spikes in the beam fluence and more faithfully characterize the continuous wave LDT of the product. Images of the sample surface were recorded before and after laser exposure using a 100x reflective microscope with Nomarski objective and examined for signs of laser damage. Damage was also identified by monitoring the power passing through the LWIR polarizer using a Laser Precision Meter Rk-5720 power ratiometer with Laser Probe Rk-570 pyroelectric power head and integrated chopper. An Ophir 150C-sh thermopile detector head with SH-USBI interface was used to measure incident laser power and passing-state transmittance. High LWIR polarizer contrast was verified using the same laser and detectors. For the MWIR product, a Spectra Physics 1064nm HIPPO laser operating at 25 kHz was used to pump a PPLN OPO for 7 ns pulses at a wavelength of 3.3 μm with a $1/e^2$ beam diameter was 150 μm. The samples were tested with the aluminum ribs facing the incoming laser beam in the passing and blocking polarizer orientations. Bare AR-coated samples, without the wire grid, were also tested.

2.5 Sample analysis

Samples were characterized in plan-view and cross-section (after cleavage) by SEM. It was found that a further investigation of the cross-sections by STEM was needed for improved resolution of the finer-scale sample features. Cross sectional STEM lamellae were prepared by a focused ion beam (FIB) in-situ lift-out technique using an FEI Nova 200 Dual Beam instrument. Samples were then observed in bright and dark field using a Hitachi HD-2000 STEM instrument operating at 200 kV. Laser damage threshold samples were analyzed using a reflective microscope and Nomarski objectives ranging in power from 5x to 50x magnification. The LWIR sample was also examined using the electron beam of the FEI Nova instrument in plan-view and at 54-58° AOI after FIB milling. Two types of platinum infiltration were performed before all FIB milling to protect the delicate wire grid structure from beam damage.

2.6 Optical modeling

Rigorous Coupled Wave Analysis (GSolver® version 4.20b) was utilized in optical modeling of the silicon IR products from wavelengths of 1.5 to 10.0 μm (MWIR product) or 1.5 to 17.5 μm (LWIR product) in 50 nm increments. The model incorporated silicon IR optical constants generated by J.A. Woollam from coupled IR-VASE and transmittance analysis of a series of uncoated silicon parts.[5] The model also utilized the aluminum optical constants labeled "Al-IR, 2-33um, Genosc", which were derived from an earlier IR analysis based on a generic oscillator model and provided by J.A. Woollam. AR-coating data provided by the coating vendor was also input into the optical model to account for the reduced silicon reflectivity. For modeling purposes a simple rectangular wire cross section was assumed, with the metal duty cycle fixed at 27.8% (40 nm) of the wire grid pitch (144 nm). The wire height was set to 165 nm, giving an aspect ratio of about 4.1 to 1. In addition to the real zero-order propagating modes, convergence of the RCWA solutions was observed with inclusion of only +/- 12 reflected and +/-12 transmitted evanescent diffracted orders. Simple initial transmittance simulations for the SIR3-5 and SIR7-15 products were performed by multiplying the zero order RCWA transmittance results of the first and second models, depicted in figure 3. The first model utilized a semi-infinite air superstrate followed by the WGP layer, AR-coating layers, 0.62 mm thick silicon layer, and a semi-infinite silicon substrate. This model's transmittance results include the wafer's front-side WGP, AR-coating, and silicon surface reflections as well as absorption from the WGP, topside AR-coating layers, and the silicon substrate. The second model utilized the same semi-infinite superstrate and semi-infinite substrate with AR-coating layers in-between and accounts for the reflective losses from the backside of the wafer. Internally reflected beam effects were ignored. For reflectance modeling, the backside wafer reflectance was ignored as it is small within the AR-coating design region. Later, more complete transmittance simulations for the SIR7-15 product did account for the non-coherent backside and internal reflections between wafer surfaces by incorporating the effects of a third model, with semi-infinite silicon superstrate, 0.62 mm thick silicon layer, AR-coating layers, WGP layer, and semi-infinite air substrate. For non-normal AOI calculations in the third model, the illumination (I_o) comes from below with an approximate internal angle based on

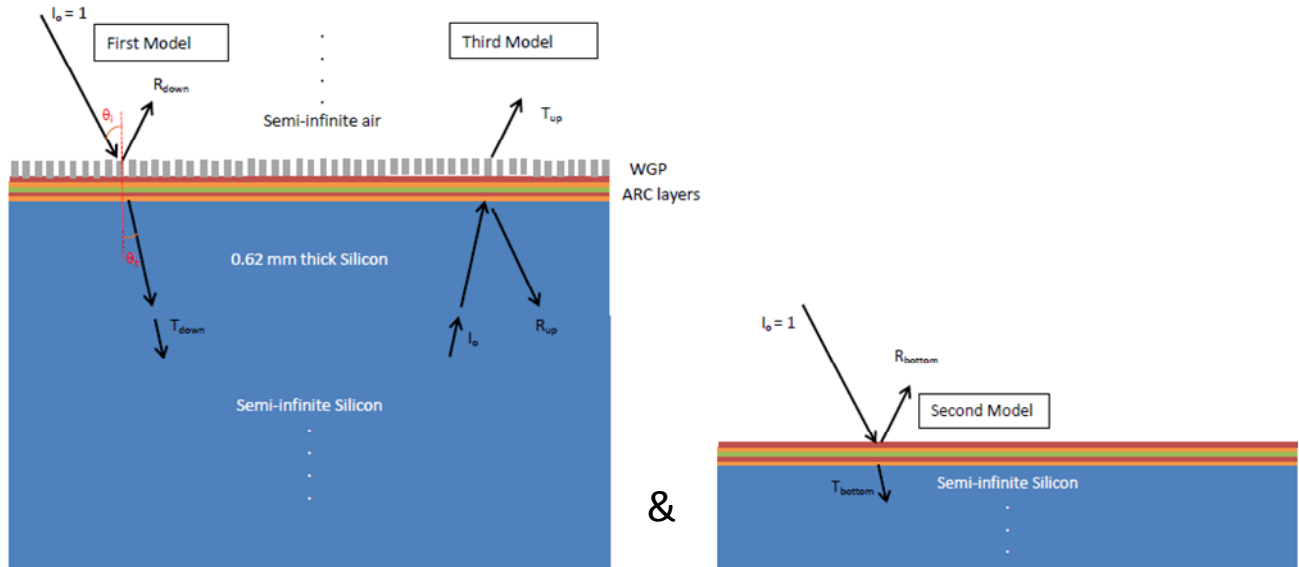Snell's Law and a fixed silicon index of refraction (n = 3.4). Incorporating all internal reflections into the LWIR

Figure 3. RCWA modeling schematics showing the various layers, incoming beam direction I_o, and the important outputs for the three simulations used to calculate WGP product response. Combining results from the various models allows for the effects of various internally reflected beams to be included.

modeling generated the geometric series shown in equations 1 & 2,

$$R_{total} = R_{down} + T_{down} \cdot R_{bottom} \cdot (R_{up} \cdot R_{bottom})^0 \cdot T_{up} + T_{down} \cdot R_{bottom} \cdot (R_{up} \cdot R_{bottom})^1 \cdot T_{up} + T_{down} \cdot R_{bottom} \cdot (R_{up} \cdot R_{bottom})^2 \cdot T_{up} + ... \quad (1)$$

$$= R_{down} + T_{down} \cdot R_{bottom} \cdot T_{up} \cdot (1 - R_{up} \cdot R_{bottom})^{-1}.$$

$$T_{total} = T_{down} \cdot (R_{bottom} \cdot R_{up})^0 \cdot T_{bottom} + T_{down} \cdot (R_{bottom} \cdot R_{up})^1 \cdot T_{bottom} + T_{down} \cdot (R_{bottom} \cdot R_{up})^2 \cdot T_{bottom} + ... \quad (2)$$

$$= T_{down} \cdot T_{bottom} \cdot (1 - R_{up} \cdot R_{bottom})^{-1}.$$

where the subscript *total* refers to the total transmittance (T) or reflectance (R) and the subscripts *down*, *bottom*, and *up* refer to the RCWA results from the first, second, and third models respectively. Including these internal reflections allows for realistic modeling of the WGP product performance for light sources with small low coherence lengths, where interference effects between the front and back of the silicon substrate are negligible. The RCWA Modeling was performed at varying AOI (0°, 12°, 45°), and the s-type reflections were chosen such that the polarization direction is aligned with the wires while the p-type reflection is orthogonal to the wires, hence R_s is the blocking state reflectance while R_p is the passing state reflectance. This nomenclature not only provides a distinction for the normal incidence reflections, but the configuration gives improved performance in polarizing beam-splitter applications.

3. MEASUREMENT RESULTS AND DISCUSSION

3.1 Overview

FTIR normal incidence transmission analysis of Moxtek IR polarizers showed excellent contrast results between blocking and passing states (>37 dB over the design wavelengths). For the MWIR product, passing state transmittance was typically >95% between 3.8 and 5.5 μm. Due to absorption from oxygen impurities in the AR-coating, passing state transmittance drops at the shorter wavelengths, but remains above 85% at 3 μm. Silicon IR absorption limits the passing state transmittance for the broadband LWIR product to a range of 68-93% for the 7-15 μm AR-coating design region. A narrowband AR-coated WGP for 7.5 μm wavelength transmits 94% of the passing state while maintaining a contrast ratio of better than 42dB while a polarizer in development for the 10.6 μm CO_2 laser line shows 84% transmission in the passing state and a contrast ratio of about 45 dB. RCWA modeling results for normal incidence transmission and 12° angle of incidence reflectance of the broadband MWIR and LWIR polarizers matched the general trends observed in the corresponding FTIR experiments. For the broadband LWIR product, preliminary LDT testing indicates that damage was

being initiated at defects introduced during silicon AR-coating. In the blocking state, the LWIR product could withstand 100 kW/cm^2 of continuous wave CO_2 laser radiation at 10.6 µm wavelength, while the parts showed an order of magnitude lower laser damage threshold in the passing polarization state. The Moxtek MWIR polarizer has an improved AR-coating and does not show the same damage initiation mechanism. The MWIR product showed a LDT of 650 W/cm^2 in the blocking state and better than 14 kW/cm^2 in the passing state at a wavelength of 3.3 µm.

3.2 FTIR transmission experiments

Table 1 depicts current minimum Moxtek SIR Product performance criteria for passing state transmittance (T_p) and polarizer contrast ratio (T_p/T_s). Figure 4 depicts FTIR normal incidence T_p measurement results for Moxtek Silicon IR products, as well as results for passing and blocking state (T_s) transmittance of the SIR7-15 (LWIR) product at varying AOI. Due to LWIR silicon absorption features, the SIR7-15 polarizer T_p performance is limited by substrate thickness. The performance crossover between SIR3-5 and SIR7-15 products is at ~7.2 µm wavelength and 84.4% T_p, but fig. 4b shows AR-coating performance can be tuned to shorter wavelengths by changing the angle of incidence. Arranging the SIR7-15 polarizer to operate at 45° AOI shifts the performance crossover with SIR3-5 to ~6.8 µm and 87.3% T_p.

Product	Wavelength (µm)	Minimum T_p	Minimum Contrast Ratio	
SIR3-5	3.0 - 3.7	85%	5,000 (37 dB)	
	3.7 - 5.0	94.5%	7,000 (38.5 dB)	
SIR7-15	7.0 - 8.8	78%	7,000 (38.5 dB)	
	8.8 - 15	68%	10,000 (40 dB)	
	10.6	82%	11,500 (40.6 dB)	
SIR7.5*	7.5	92%	7,000 (38.5 dB)	* developmental products
SIR10.6*	10.6	83%	11,500 (40.6 dB)	

Table 1. Minimum passing state transmittance (T_p) and contrast ratio for Moxtek SIR Products at normal incidence.
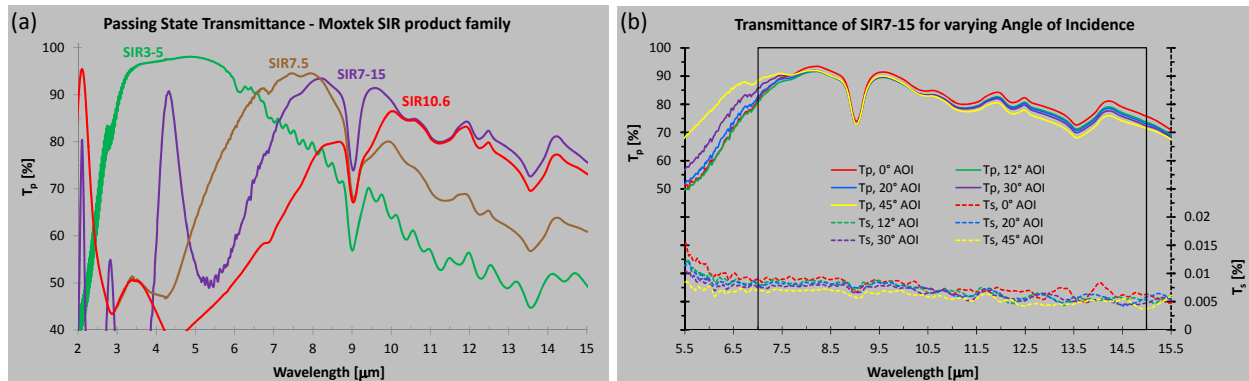

Figure 4. (a) Passing state transmittance (T_p) at normal incidence for broadband MWIR (**SIR3-5**) and LWIR (**SIR7-15**) polarizers and narrow band developmental polarizers **SIR7.5** and **SIR10.6**. (b) Transmittance for passing state (T_p, solid colored lines and left ordinate) and blocking state (T_s, dashed colored lines and right ordinate) for the LWIR (SIR7-15) product at varying angle of incidence (AOI) (**0°**, **12°**, **20°**, **30°**, and **45°**).

As mentioned in Section 2.2, the varying AOI scans did not utilize a compensating substrate to shift the beam back to the same position as the baseline measurement, so there could be slight shifts in transmittance results due to non-uniformity of the DLaTGS detector. The chosen aperture setting gave a fairly high intensity beam with about a 7.4 mm diameter in the center of the compartment. The chosen aperture allowed for a low gain setting while still utilizing most of the dynamic range of the detector. This allowed small signals to be measured in the blocking state polarizer configuration with reasonable noise levels, but the large beam may have also filled the detector enough that beam shifts could impact the quantitative accuracy of T_p at varying AOI. The fact that T_p decreases at longer wavelengths but increases at shorter wavelengths for increasing AOI provides some confidence that the measured effects are real, as this trend matches the modeling predictions of section 3.6. If the effect were solely due to the edge of the beam shifting off of the detector, then one would expect a similar decrease in T_p at all wavelengths. Since T_p and T_s beams should both shift in the same way with increasing angle of incidence, the polarizer contrast ratio between passing and blocking states should be less sensitive to beam shift. These results are presented in figure 5(a) and (b) for MWIR and LWIR products respectively.

The FTIR instrument noise floor limited transmission measurement in the blocking state, but the maximum measurable contrast ratio (5:1 signal to noise) was still better than 40 dB between 3 and 15 μm for the Nexus 870 using 256 scan averaging and slightly better for the CARY 670, which allowed a reduction in scan averaging to 128 scans. Based on the chosen scan averaging (and resolution settings) for the Nexus 870 (6cm^{-1}) and CARY 670 (4cm^{-1}), the T_s scans still had
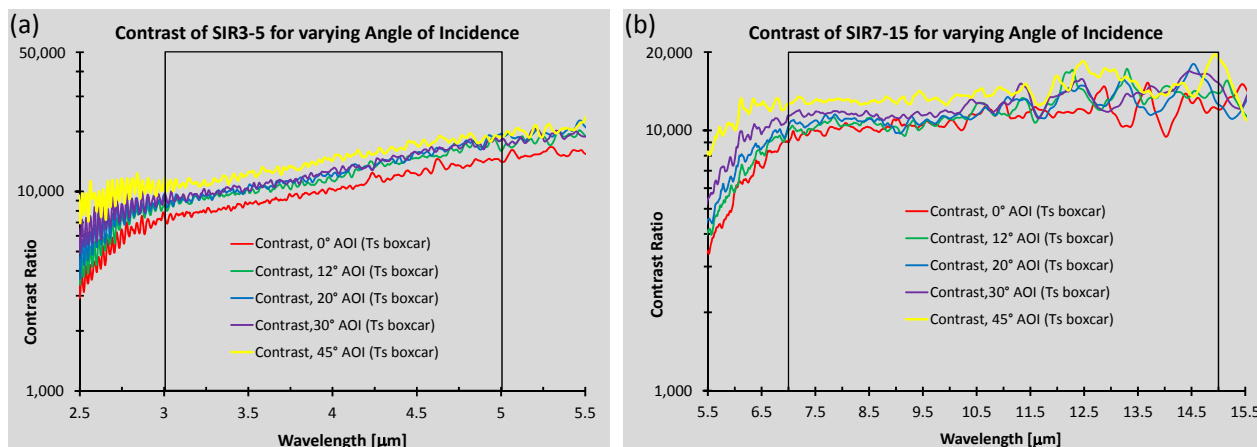

Figure 5. Contrast ratio (T_p/T_s) for (a) SIR3-5 and (b) SIR7-15 polarizer products at varying AOI (0°, 12°, 20°, 30°, and 45°).

to be smoothed using boxcar averaging, with a convolution kernel varying in size from 1 x 5 to 1 x 9, in order to produce the contrast curves shown in figure 5. At normal incidence the MWIR product maintained a contrast ratio of better than 37.8dB from 3-8 μm, while the LWIR sample exceeded 39.8 dB from 8-15 μm. The best performing LWIR sample (not depicted) had an average contrast ratio of about 43.1 dB from 7-15 μm as measured on the Nexus 870 FTIR. High contrast for the LWIR product was verified at Spica Technologies using laser sources and showed micro-spot contrast ratios ranging from 40.5 to 48.1 dB at 10.6 μm wavelength with a typical contrast of about 45 dB. The narrowband 10.6 μm polarizer was analyzed with the CARY 670 FTIR using a 5mm hard aperture and also showed a contrast ratio of about 45 dB. A CARY 5000 dual-beam dispersive spectrometer was used in an attempt to validate SIR3-5 transmittance and contrast between 2.7 and 3.3 μm, however due to drift in the source power and/or detector responsivity and possible detector non-linearity, the data only shows good agreement below 3 μm and is excluded for brevity.

3.3 FTIR reflection experiments

Figure 6 presents polarizer reflectance measurements at 12° angle of incidence (AOI) using the CARY 670 FTIR and Harrick absolute specular reflectance accessory, as well as some modeling results discussed in section 3.6. Proper tuning of the input polarization state allows for R_p^2 and R_s^2 to be directly measured at 12° AOI, as described in section 2.3. Much of the slight disagreement between modeling and theory is likely a result of improper pre-analyzer alignment. According to Harrick Scientific,[6] vertically polarized light is rotated differently than horizontally polarized light through their specular reflectance accessory. Since fine alignment of the pre-analyzer orientation was only performed for the R_s^2 measurement, the R_p^2 measurements evidently had a beam polarization that was rotated slightly (~10°) from the optimal orientation. The "VW" method for R^2 measurements also assumes that there is no depolarization of the beam by the sample in reflectance, which is only true if the pre-analyzer is properly aligned and the beam is of high purity. Although the aluminum beam steering mirrors of the Harrick accessory have only a weak dependence on polarization orientation, this depolarization effect will also bias the second sample reflection further towards the s-polarization state. These factors help explain why the R_p measurements are slightly larger than the modeling results. The reduced R_s compared to modeling in figure 6b for the SIR7-15 polarizer could be due to scattering from defects introduced during AR-coating. Reflectance measurements at 45° AOI were also taken for MWIR and LWIR products, but due to the sample and alignment dependent mix of *s*- and *p*-type and blocking- and passing-state reflections, quantitative comparison between modeling and experiment was not undertaken.

(a) **Moxtek SIR3-5 WGP 12° Reflectance vs. modeling**

(b) **Moxtek SIR7-15 WGP 12° Reflectance vs. modeling**

— modeled Rs, 12°AOI
-- measured Rs, 12°AOI
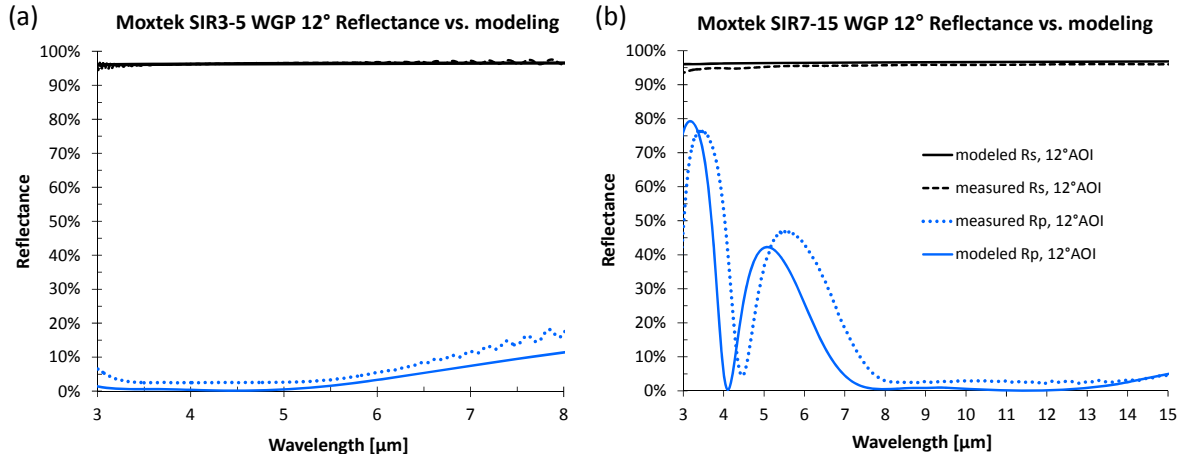···· measured Rp, 12°AOI
— modeled Rp, 12°AOI

Figure 6. FTIR 12° angle of incidence reflectance measurement results for (a) MWIR and (b) LWIR broadband WGP products. Solid and dashed or dotted lines denote reflectance modeling and experimental measurements respectively. **Black** lines indicate *s-type* reflections in the blocking polarizer state and **blue** lines indicate *p-type* reflections in the passing state.

3.4 Laser damage threshold testing

Preliminary Laser Damage Threshold (LDT) test results are presented in Table 2 for the broadband Moxtek WGP products and for the bare AR-coated silicon substrates. The passing and blocking columns refer to the polarizer orientation with respect to the laser beam's incoming polarization state. Figures 7 and 8 in the following section present optical reflectance and scanning electron microscope images of un-exposed and exposed regions of the LWIR WGP sample, and demonstrate that damage was preferentially initiated at pre-existing defects in the AR-coating.

	LDT Results [kW/cm²]		Pulsed LDT Results [J/cm²]		LDT Test Parameters					
Product / Description	blocking	passing	blocking	passing	λ [μm]	test type	Pulse Duration	Rep Rate [kHz]	1/e² Beam Diameter [μm]	Exposure duration
SIR_7-15μm WGP	100	10	--	--	10.6	cw	--	--	360	30 sec.
7-15μm AR-coated substrate	--	397	--	--	10.6	cw	--	--	124	60 sec
SIR_3-5μm WGP	0.646	>14	0.026	> 0.56	3.3	pulsed	7 ns	25	150	20 min.
3-5μm AR-coated substrate	--	>14	--	> 0.56	3.3	pulsed	7 ns	25	100	12 msec.

Table 2. Preliminary Laser Damage Threshold (LDT) test results for SIR WGP Products and bare AR-coated silicon substrates.

For the broadband LWIR product in the passing state the wires can withstand 10 kW/cm² of continuous wave 10.6 μm CO_2 laser radiation for 30 s, while the parts showed an order of magnitude larger LDT for the blocking polarization state (100 kW/cm²), except in some defective regions of the AR-coating, where damage was again apparent at about 10 kW/cm². These samples were tested with the aluminum wires facing the incoming laser beam, and hence in the blocking configuration the wire grid reflects about 95% of the incident radiation, which appeared to help protect some of the AR-coating defects from laser damage. However some types of AR-coating defects, such as the one depicted in figure 8(a), can result in openings in the wire grid. These types of defect sites evidently become damaged at the lower fluence of 10 kW/cm², even when exposed to a laser in the blocking polarization state.

The SIR3-5 (MWIR) WGP and both of the bare AR-coated substrate samples (without wire grid) came from subsequent vendor lots with improved AR-coatings and did not show the same laser damage initiation mechanisms. The bare 7-15 μm AR-coated substrate showed a LDT of 397 kW/cm² with no damage at ten separate sites, each with 60 s exposure duration. The bare 3-5 μm AR-coated substrate could not be damaged using the OPO setup described in section 2.4, which had a maximum fluence of 14 kW/cm². The sample showed no damage at ten separate sites, each with a 300 pulse (12 ms) exposure. For the SIR3-5 WGP product, preliminary pulsed LDT testing using 20 minute exposures at 3.3 μm wavelength indicated the wires can withstand better than 14 kW/cm² in the passing state (no damage observed at five sites), but only ~650 W/cm² in the blocking state. Evidently the Al nanowires absorb enough at 3.3 μm wavelength that the pulsed laser causes damage at a much lower average fluence in the blocking state than it does in the passing state.

3.5 Sample analysis

From SEM and STEM images (figures 1c and 1d), it is evident that the etched aluminum wires do not have the rectangular cross section assumed in the optical modeling. From STEM analysis of the initial broadband LWIR product run, the wire width varied from about 30-60 nm over the cross section and the wire height was about 190 nm. STEM analysis of the MWIR product revealed a wire width varying from 25-55 nm over the cross section and a wire height of 160-165 nm. For simplicity all modeling assumed 40 nm wire width and 165 nm tall wires. A thin native aluminum oxide is also evident on the outside of the wires for both products, but was not modeled.

Figures 7 and 8 present optical reflectance and scanning electron microscope images of un-exposed and exposed regions of the LWIR WGP sample used in LDT testing. As depicted by the black arrows in figure 7, reflectance microscopy revealed that damage was initiating and spreading from defects in the AR-coating. Figure 7(a) and (b) depict a defective sample region before and after exposure with 20 kW/cm^2 beam fluence and the polarizer oriented in the passing state, while figure 7(d) and (e) depict a similar defective sample region before and after exposure with 110 kW/cm^2 beam fluence, but with polarizer oriented in the blocking state. The defects appear to darken under the reflectance microscope and in the blocking state, the laser leakage through the part tended to increase. For instance, during a 30 s exposure with 110 kW/cm^2 beam fluence in the blocking state, the beam leakage through the polarizer increased by a factor of ~36. Presumably most of this increased leakage would be due to damage to the wire grid covering the AR-coating defect. At beam fluence larger than 110 kW/cm^2, or during longer exposures, the damage in the blocking state began to propagate away from the defects and into the rest of the wire grid structure, as depicted in figure 7 (f). On the contrary, for the passing polarization state, figure 7 (c) appears to show that laser damage remains confined around defects in the AR-coatings. However, figure 8 images (e) and (f) depict a similar passing state laser damage spot and reveal increased cracking in the wire grid and perhaps in the underlying AR-coating.
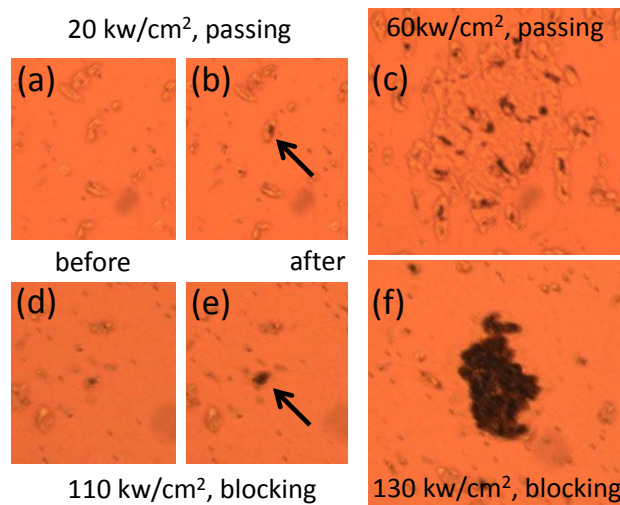

Figure 7. 100x reflective microscope images of preliminary LDT results for a defective LWIR WGP sample in passing (a-c) and blocking (d-f) states before (a, d) and after (b-c, e-f) exposure for 30 s with beam intensity near (a-b, d-e) and above (c, f) the corresponding LDT. The black arrows indicate preferential damage at pre-existing AR-coating defects.

The type of AR-coating defects evident before exposure in figure 7(a) and (d) are displayed at higher magnification in the SEM images of figure 8(a)-(c). The AR-coating can have cracks, as in image 8(a), causing discontinuities in the wire grid or merging of nanowires. Image 8(b) reveals a more subtle form of damage, which only results in merged wires. As evident in image 8(c), there are also some round eruptions or deposits, presumably from the AR-coating process, which can result in a solid aluminum films. The SEM image in figure 8(d) was taken after LDT testing with similar exposure parameters to the damage spot depicted in figure 7(c), and clearly demonstrates darkening of the defects and damaged region. Figures 8(e)-(f), higher magnification images of the same damage spot, reveal cracking around, and perhaps underneath the defects, as well as melting and merging of aluminum nanowires above the AR-coating defects.
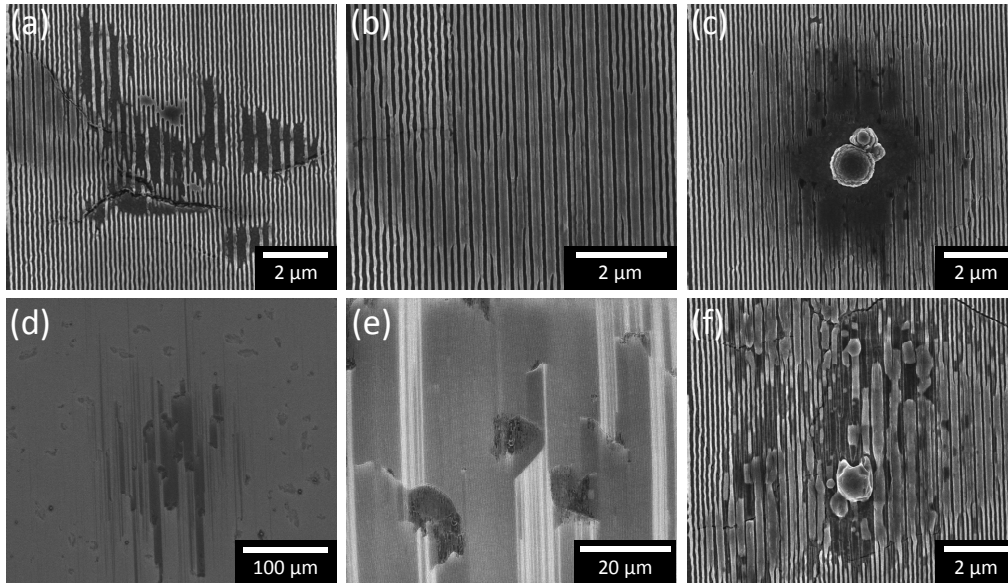
Figure 8. Plan view SEM images of a LWIR passing state WGP sample in an unexposed region (a-c) where various defects in the AR-coating have impacted the wire grid structure, and in an exposed region (d-f), with increasing magnification.

Figure 9 reveals a laser damage spot of the LWIR WGP in the blocking state where the fluence was low enough that damage includes oxidation and melting, but not ablation. As evident in figure 9(e), which corresponds to the higher magnification region of figure 9(d) outlined in blue, the wires appear to thicken and then merge into larger globular structures. The wavy pattern of globules evident in figure 9(a) and (b) might correlate to the higher intensity regions of a laser beam spot that contains some interference fringes instead of a uniform Gaussian laser beam profile. The white arrows in figure 9(a) depict AR-coating defects in an undamaged region of the sample, similar to those in figure 8(a)-(c).
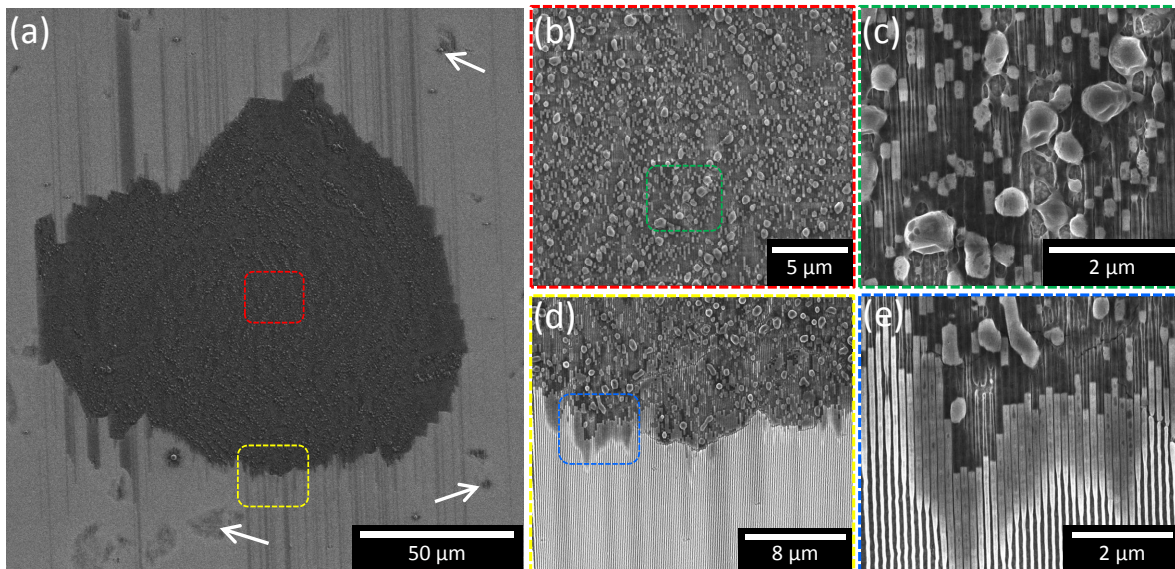

Figure 9. Plan view SEM images of a laser damage spot from LDT testing of a defective LWIR WGP in the blocking state. Magnification increases from left to right. The white arrows point to defects in the AR-coating outside of the damaged region. Images (b)-(c) depict the center while (d)-(e) depict the edge of the damage spot.

Figure 10 depicts a Pt-infilled, FIB-milled SEM cross section of the lower right edge of the same LDT spot depicted in figure 9(a). Rows (a)-(c) of figure 10 span the edge of the damage spot from right to left respectively. The rightmost nanowires in row (a) are clearly not impacted significantly by the blocking state laser exposure, although e-beam

charging during SEM focusing has made some wires brighter than others. The wires begin to deform into a more round cross section towards the middle of row (a). The interiors of the nanowires in this damaged region must have become molten, as clearly the aluminum content of some of the nanowires has been expelled, which evidently leaves behind an empty oxide shell that is not infilled by Platinum during preparations for sample cross-sectioning. The molten aluminum appears to erupt from the nanowire oxide shell and collect into larger droplet-like structures, perhaps in an attempt to reduce surface tension. There is also cracking in the AR-coating layers beneath the wires associated with these phase changes and mass transport processes.
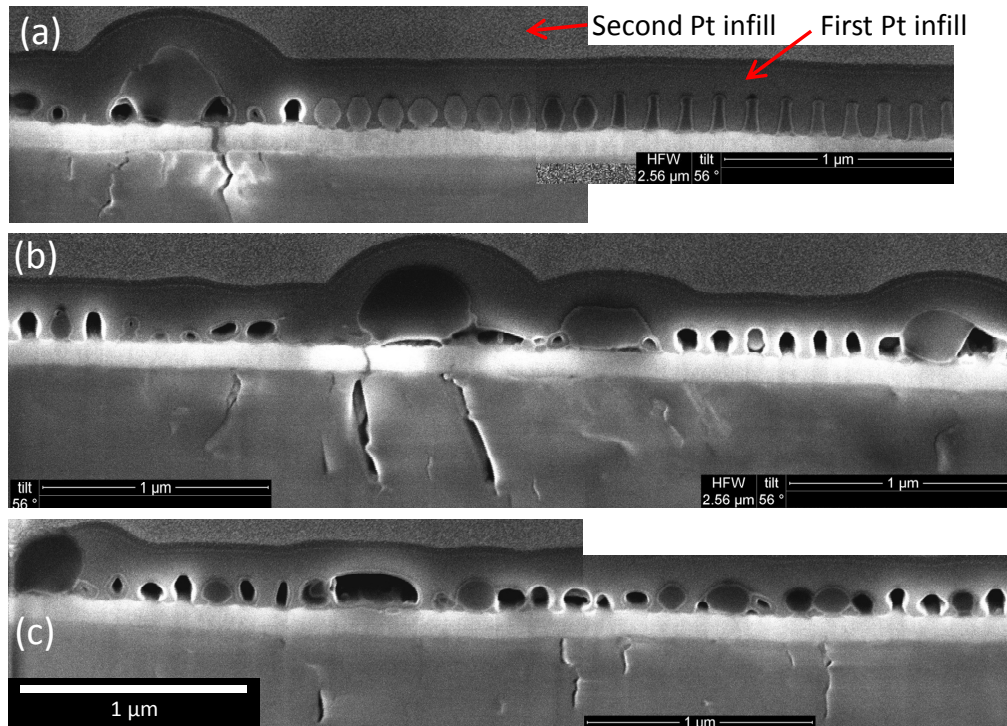

Figure 10. Platinum-infilled, FIB-milled SEM cross section of the edge of a damage spot from a defective LWIR WGP after blocking state laser exposure. Rows (a)-(c) span the edge of the damage spot from right to left respectively.

Figure 11 depicts plan view SEM images of a blocking state LWIR WGP damage spot that was caused by a 2 s exposure with laser beam intensity of 120 kW/cm^2. In this case, the CO_2 laser itself was operating at low power and without a partial reflector, which evidently results in more carrier wave modulation of the instantaneous beam energy and more of a pulse-like operation mode. The high peak power that the WGP was exposed to in this mode resulted in complex morphology, which likely includes processes such as oxidation, melting, evaporation and/or ablation, and material ejection and/or vapor phase condensation. The center and edge of the damage spot, depicted in images 11(b) and (c) respectively, appears to have a re-solidified topography with some large-scale cracking, while lacey deposits are evident with decreasing density at larger distances from the central damaged region in images (d)-(f).

Figure 12(a) shows the same damage spot depicted in figure 11(a), but at a 54° tilt angle after FIB-milling two cross sections. Figures 12(b)-(d) depict high magnification images of the rightmost cross section, which corresponds to a region similar to the one depicted in figure 11(e). The pulse-like exposure has caused cracking in the AR-coating, as depicted in figure 12(b). A shell, possibly composed of aluminum oxide, is clearly evident around the deformed nanowires and along the substrate between the wires in figure 12(c). It appears the stresses caused by the melting of the aluminum wires is beginning to lift this shell layer up off of the substrate, which allows adjacent molten aluminum to merge together as depicted in figure 12(d). The FIB-milled cross section in figure 12(d) depicts deformed and merged nanowires wires under the type of lacey debris shown in figure 11(d), thus the debris was likely generated in another region of the damage spot as the wires are still evident in the cross section. It appears the aluminum nanowires may have oxidized and broken apart due to some rapid laser-induced process and been ejected into the air above the center of the damaged spot. The segregation based on effective particle size depicted images (d)-(f) may have occurred while the material settled back onto the substrate.
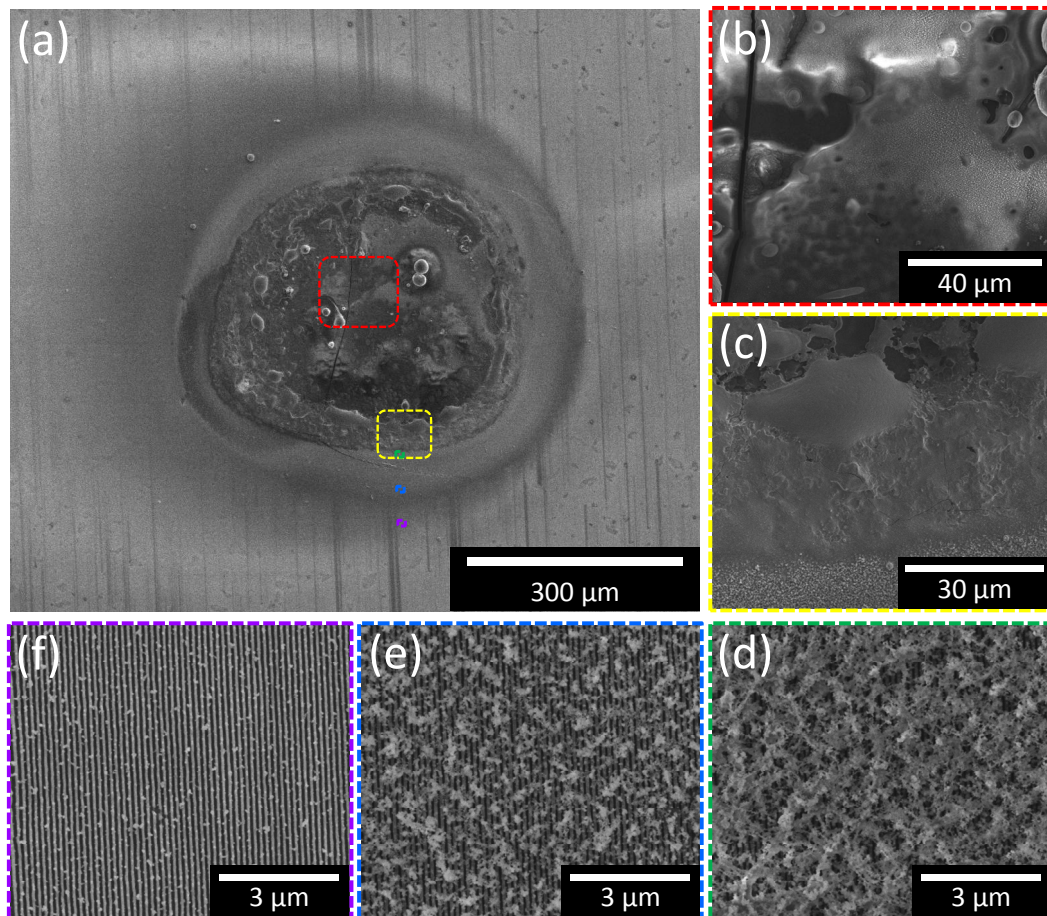
Figure 11. Plan view SEM images of a damage spot from testing of a defective LWIR WGP with a pulse-like laser beam in the blocking state with intensity above the LDT. Images (b) and (c) are high magnification views of the center and edge of the damage spot while (d)-(f) are higher magnification images taken at increasing distance from the central damaged region.

As discussed in section 3.4, subsequent vendor AR-coatings lots for the SIR WGP products showed greatly improved cosmetic quality. Because of the scarcity of AR-coating defects, these subsequent lots did not show the same laser damage initiation mechanisms and show greatly improved LDT values. The bare 7-15 μm AR-coated substrate from one of these lots showed a LDT of 397 kW/cm^2 at 10.6 μm wavelength, which is 40 times larger than the corresponding passing state LDT for the WGP with defective AR-coating. Figure 13 presents plan view (a)-(b) and cross-sectional (c)-(d) SEM images of this bare 7-15 μm AR-coated silicon substrate after laser exposure with a beam intensity greater than 440 kW/cm^2. These images demonstrate different damage mechanisms than the WGP samples, which include blistering at the surface of the top AR-coating layer, some slight delamination between buried layers, and perhaps some internal voiding in one of the buried AR-coating layers. The topmost grainy layer in figure 13(c) is the Platinum that was deposited before FIB sectioning. In the future, new WGP samples will be created on the improved LWIR AR-coatings for additional LDT testing in the passing and blocking polarizer configurations.
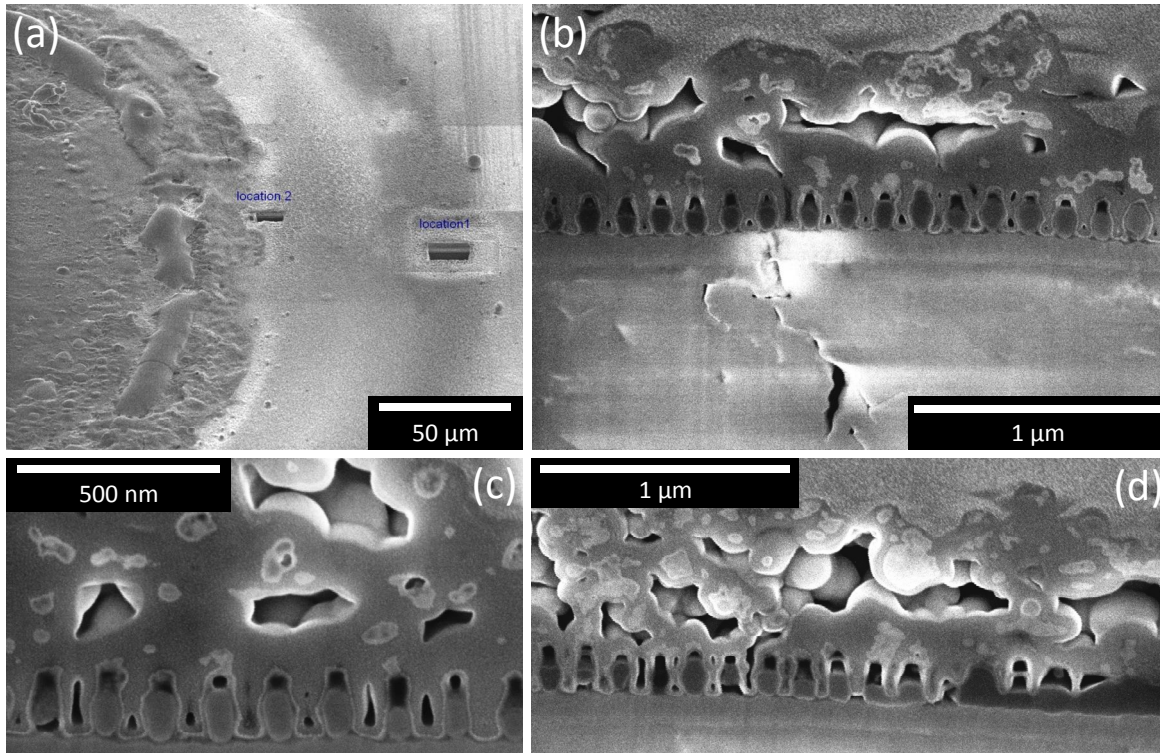
Figure 12. FIB-milled cross-sections of the same laser damage spot depicted in figure 11. Images (b)-(d) are high magnification views of the right cross-section, which is from a region similar to the one depicted in image 11(e).
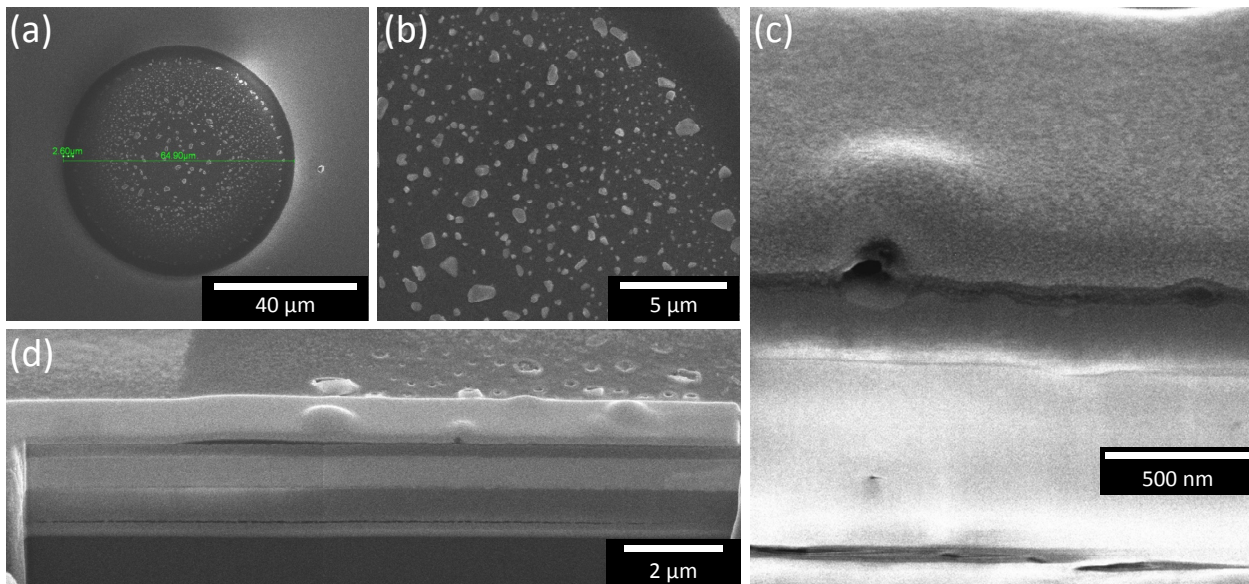

Figure 13. Plan view (a)-(b) and FIB-milled cross-sections (c)-(d) of a bare LWIR AR-coated substrate after Laser Damage Threshold testing. Images (b) and (c) are higher magnification views of the upper-right and central regions depicted in (a) and (d) respectively. The top layer in (c) is the Platinum deposited before FIB sectioning.

3.6 Optical modeling

Figure 14 presents the passing state experimental transmittance results at various AOI for the MWIR (a) and LWIR (b) broadband WGP products, and compares this to the corresponding optical modeling results described in section 2.6. The MWIR product shows good agreement between the simple transmittance modeling and measurements except at the shorter wavelengths where oxygen impurities in the AR-coating are likely decreasing performance. For the broadband LWIR transmittance measurements, large interference fringes appear at wavelengths shorter than the 7-15 µm AR-coating design region and are reproduced fairly well by the more complex modeling that was based on combining the three RCWA models depicted in figure 3 using equations 1 and 2. The LWIR WGP modeling shows larger average transmittance in the passing state when compared to the best experimental case. Errors in the fit could be due to the use of improper optical constant data in the infrared, the omission of native oxides from the modeling,[2] or the use of improper thickness for one or more simulation layer, most likely the silicon substrate. Geometrical parameters such as metal wire width and shape are also approximated in the model by a rectangular cross section, which disagrees with the SEM and STEM analysis results. The silicon optical constants used in the modeling were based on an analysis of double-side polished silicon performed by J.A. Woollam using coupled IR-VASE and transmission measurements, which showed a slightly lower value of the silicon infrared index of refraction than the value extrapolated from the well-cited analysis of Herzinger et.al.[7] This could impact the modeling in terms of AR coating performance. The bare silicon wafer thickness utilized in the J.A. Woollam characterization of optical constants was measured as 0.62 mm, and was also assumed in the RCWA modeling, but this is about 7% thinner than the typical silicon WGP production wafers so the increased path for absorption could explain the reduced experimental T_p values. The figure 14 results show little change in performance when moving away from normal incidence, although the pass band for the AR-coating shifts to shorter wavelengths at larger AOI. As mentioned in section 3.2, tuning the WGP angle of incidence is one way to improve T_p performance at shorter wavelengths where application permits. The slight experimental drop in T_p performance between 0° and 12° AOI is not evident in the modeling and might be due in part to internally reflected beams that are transmitted through the sample, which could be collected efficiently at the detector at normal incidence, but not at 12° and 45° AOI.
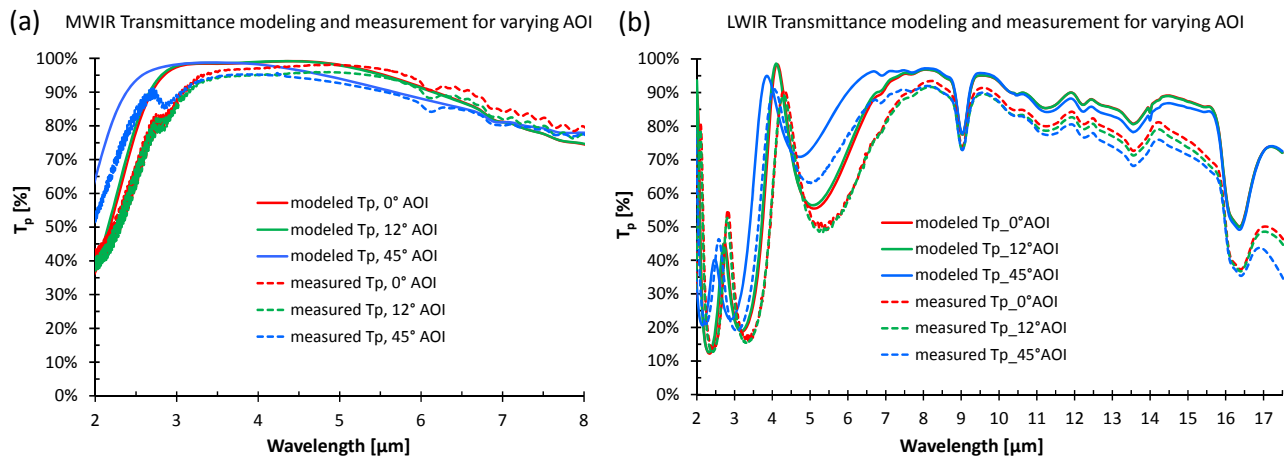

Figure 14. Optical modeling (——) and measurements (- - - -) of passing state transmittance for MWIR (a) and LWIR (b) broadband WGP products at varying angle of incidence (**red**: **0°**, **green**: **12°**, **blue**: **45°**).

Figure 15(a) depicts broadband contrast ratio (T_p/T_s) modeling at varying AOI for both the SIR3-5 (MWIR) and SIR7-15 (LWIR) WGP products based on the simple and more complex models respectively, as described in section 2.6. The LWIR product shows the same interference fringes in contrast that are evident in T_p and appears to also be a serviceable narrowband polarizer in two spectral regions, one in the MWIR around 4 µm and the other in the SWIR around 2 µm. In comparing figure 15(a) and figure 5(a) results, the measured and simple model for MWIR contrast agree fairly well below 4 µm, but diverge at longer wavelengths, especially for contrast ratios above 10,000:1. The LWIR contrast modeling results are significantly larger than the corresponding measurements at varying AOI, although alternate LWIR WGP samples have shown approximately twice the normal incidence contrast as the sample measured and presented in figure 5(b). In addition, the sample used in LWIR LDT testing was measured at Spica Technologies using a Synrad CO_2 laser source and showed roughly half the T_s value (double the contrast) of the FTIR measurement approach. Wire grid polarizers with contrast ratios much greater than 10,000:1 appear to be challenging the noise floor of the FTIR metrology

methods described in section 2.2. Moving the pre-analyzer and sample closer to the source and detector respectively might improve performance by reducing stray light effects. In the future a liquid nitrogen cooled detector and dispersed, chopped beam with lock-in amplifier will be used to better characterize the small T_s transmittance values of infrared wire grid polarizers in the crossed (blocking) configuration. Figure 15(b) plots the simple two-part RCWA contrast modeling results at varying AOI as well as the more rigorous three-part RCWA modeling results that use the geometric series results from equations 1 and 2. Agreement between the two contrast models is excellent except at wavelengths shorter than the LWIR AR coating design region, where internally reflected and transmitted beams become more important.
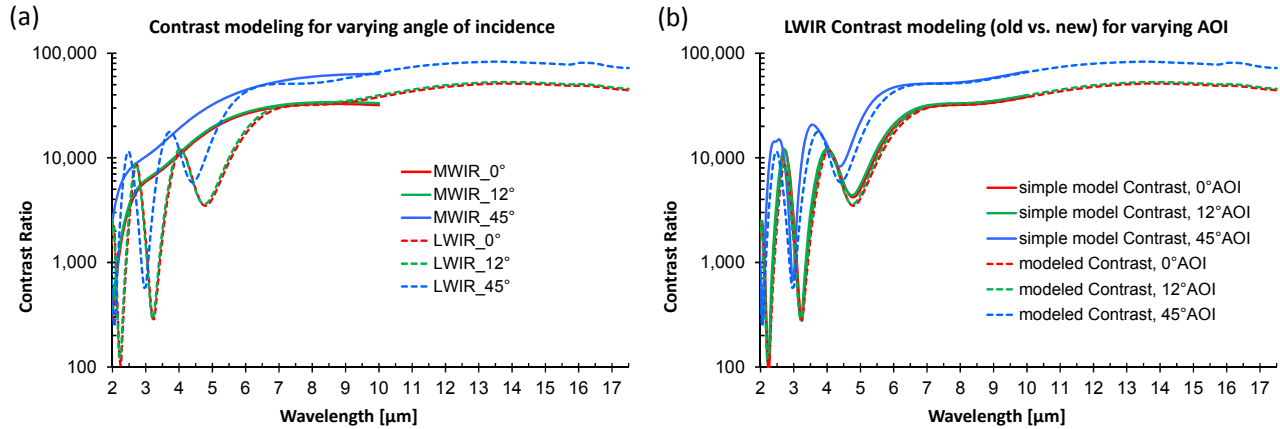

Figure 15. Contrast (T_p/T_s) modeling results for broadband WGP products at varying AOI (**red**: **0°**, **green**: **12°**, **blue**: **45°**). (a) SIR3-5 (——) and SIR7-15 (- - - -) contrast results. (b) Simple (——) and rigorous (- - - -) SIR7-15 contrast results.

Reflectance modeling results at 12° AOI for broadband MWIR and LWIR products were plotted alongside the experimental measurements in figures 6(a)-(b). As discussed in section 3.3, much of the slight disagreement between modeling and theory is likely a result of improper pre-analyzer alignment. Figure 16(a) presents broadband reflectance modeling results at varying AOI for both MWIR and LWIR products (solid and dashed lines respectively). R_s results are grouped at the top of the plot at large reflectance values, while R_p results have lower reflectance, especially in the corresponding pass bands of the respective AR coatings. The SIR3-5 (MWIR) curves utilize the simple modeling and only incorporate the front-side wafer reflections, while the SIR7-15 (LWIR) product incorporates all the wafer reflections into the model. Figure 16(b) plots LWIR product reflectance (log scale) for varying AOI using both the simple and more rigorous modeling approaches in solid and dashed lines respectively. The difference between the R_p
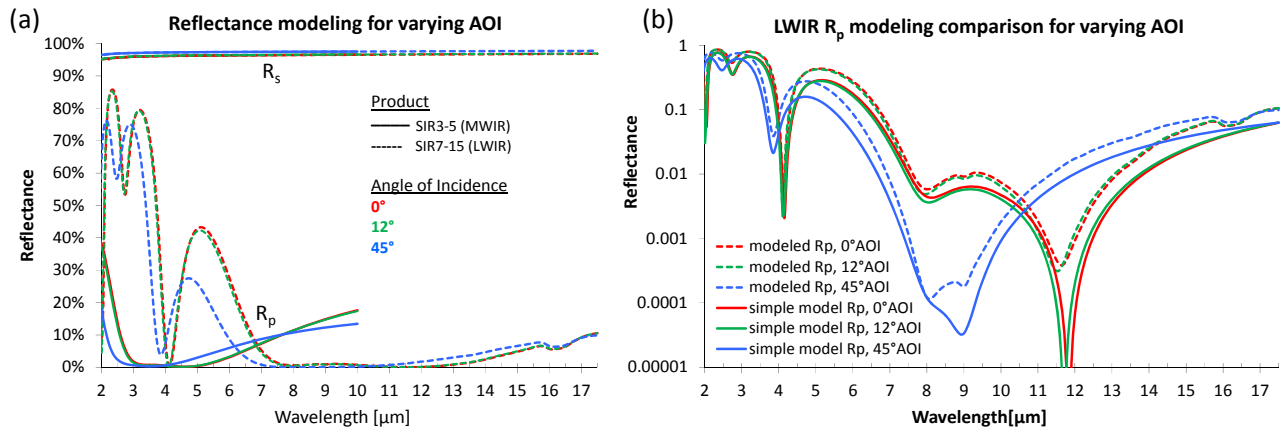

Figure 16. Reflectance modeling results for broadband SIR WGP products at varying AOI (**red**: **0°**, **green**: **12°**, **blue**: **45°**). (a) SIR3-5 (——) and SIR7-15 (- - - -) WGP reflectance. (b) Simple (——) and rigorous (- - - -) SIR7-15 R_p results.

modeling approaches is approximately a factor of two, except near reflectance nulls in the AR-coating and near silicon IR absorption peaks. This makes sense since the first term in the geometric series approach adds the first backside wafer reflection, which is similar to the front-side wafer reflection in the passing state wire grid polarizer orientation. R_s (not

plotted), showed no significant change between models as almost nothing transmits through the WGP in the blocking state to contribute to a backside reflection.

4. CONCLUSIONS

Moxtek has developed several high contrast IR polarizers on silicon suitable for mid-wavelength and long-wavelength thermal IR applications using wafer-scale aluminum nanowire patterning capabilities. The MWIR polarizer typically transmits better than 95% of the passing state between 3.8 and 5.5 μm while maintaining a contrast ratio of better than 37dB from 3-8 μm, while the broadband LWIR polarizer typically transmits between 68% and 93% of the passing polarization state between 8 and 15 μm and has a contrast ratio exceeding 38.5 dB. A narrowband AR-coated WGP for 7.5 μm wavelength transmits 94% of the passing state while maintaining a contrast ratio of better than 42dB while a polarizer being developed for the 10.6 μm CO_2 laser line shows 84% transmission in the passing state and a contrast ratio of about 45 dB. Transmission and reflectance measurements from a Fourier Transform Infrared spectrometer showed good qualitative agreement with optical modeling results from a rigorous coupled wave analysis package. Incorporating backside wafer reflections into the modeling was found to be important for accurate R_p results. At large angles, transmittance remains high for the passing state polarization except at longer wavelengths, which should maintain system efficiency even when projecting or imaging large IR sources or scenes through the polarizer using large cone angles. Tuning the beam AOI on the sample to large angles can shift the pass band of the AR coating to shorter wavelengths. The broadband LWIR polarizer also shows good narrowband performance around 2 and 4 μm. Preliminary LDT testing and sample analysis indicated that laser damage was initiated at defects in the silicon AR-coating for the LWIR product. The wires of the broadband LWIR product can withstand 100 kW/cm^2 of continuous wave CO_2 laser radiation at 10.6 μm wavelength in the blocking state, while the product shows an order of magnitude lower laser damage threshold for the passing polarization state. SEM analysis revealed several damage mechanisms for the passing and blocking configurations, including wire melting and deformation, rupture of the oxide shell, and expulsion and coalescence of aluminum into larger droplets. Cracking in the AR-coating was evident under the laser damaged regions of the wire grid. It is not clear if the cracking in the AR coating is related to the phase changes in the aluminum nanowires or if they are independent damage mechanisms. The defect level was dramatically reduced in later AR coating runs and the bare LWIR AR-coated sample showed LDT performance of 397 kW/cm^2. The Moxtek MWIR polarizer also has a low defect AR-coating and does not show the same LDT damage initiation mechanism. 7 ns pulsed laser damage threshold testing at a wavelength of 3.3 μm indicated the wires can withstand 650 W/cm^2 in the blocking state and better than 14 kW/cm^2 in the passing state.

REFERENCES

[1] Goldstein, D.H., Erbach, P., "Evaluation of infrared (3-12μm) wire grid polarizers", Proc. of SPIE 7672, 76720E (2010).

[2] Hu, C. and Liu, D., "A high-performance Aluminum wire-grid polarizer for the optical telecommunication applications", Proc. of SPIE 7134, 71344J-6 (2008).

[3] Wang, J.J., Walters, F., Liu, X., Sciortino, P. and Deng, X., "High-performance, large area, deep ultraviolet to infrared polarizers based on 40 nm line/78 nm space nanowire grids", APL 90, 061104 (2007).

[4] Yang, Z.Y. and Lu, Y.F., "Broadband nanowire-grid polarizers in ultraviolet-visible-near-infrared regions", Optics Express 15, 9510 (2007).

[5] Tiwald, T., Applications Engineer, J.A. Woollam Company, personal communications, Jan. 15 - 16, (2013).

[6] Berets, S., Applications Engineer, Harrick Scientific Products, personal communications, Mar. 12 - April 25, (2013).

[7] Herzinger et al., "Ellipsometric determination of optical constants for silicon and thermally grown silicon dioxide via a multi-sample, multi-wavelength, multi-angle investigation," JAP 83, 3323-3336 (1998).